How to cite: *Angew. Chem. Int. Ed.* **2024**, *63*, e202313591
doi.org/10.1002/anie.202313591

Conductive MOFs Hot Paper

A General Synthesis of Nanostructured Conductive Metal–Organic Frameworks from Insulating MOF Precursors for Supercapacitors and Chemiresistive Sensors

Chuanhui Huang[+], Weiming Sun[+], Yingxue Jin[+], Quanquan Guo[+], David Mücke[+], Xingyuan Chu, Zhongquan Liao, Naisa Chandrasekhar, Xing Huang, Yang Lu, Guangbo Chen, Mingchao Wang, Jinxin Liu, Geping Zhang, Minghao Yu, Haoyuan Qi, Ute Kaiser, Gang Xu, Xinliang Feng,* and Renhao Dong**

Abstract: Two-dimensional conjugated metal–organic frameworks (2D *c*-MOFs) are emerging as a unique subclass of layer-stacked crystalline coordination polymers that simultaneously possess porous and conductive properties, and have broad application potential in energy and electronic devices. However, to make the best use of the intrinsic electronic properties and structural features of 2D *c*-MOFs, the controlled synthesis of hierarchically nanostructured 2D *c*-MOFs with high crystallinity and customized morphologies is essential, which remains a great challenge. Herein, we present a template strategy to synthesize a library of 2D *c*-MOFs with controlled morphologies and dimensions via insulating MOFs-to-*c*-MOFs transformations. The resultant hierarchically nanostructured 2D *c*-MOFs feature intrinsic electrical conductivity and higher surface areas than the reported bulk-type 2D *c*-MOFs, which are beneficial for improved access to active sites and enhanced mass transport. As proof-of-concept applications, the hierarchically nanostructured 2D *c*-MOFs exhibit a superior performance for electrical properties related applications (hollow Cu-BHT nanocubes-based supercapacitor and Cu-HHB nanoflowers-based chemiresistive gas sensor), achieving over 225 % and 250 % improvement in specific capacity and response intensity over the corresponding bulk type *c*-MOFs, respectively.

Introduction

The realization of electrical conductivity in porous metal–organic frameworks (MOFs) enables them with a broad spectrum of potential applications in energetic and electronic devices, such as supercapacitors,[1] thermoelectrics,[2] catalysis,[3] chemiresistive sensors,[4] spintronics,[5] optoelectronics and superconductors,[6] which were previously unimaginable with the insulating MOFs.[7] The layer-stacked two-dimensional conjugated MOFs (2D *c*-MOFs) with in-

[*] Dr. C. Huang,[+] Dr. Q. Guo,[+] X. Chu, Dr. N. Chandrasekhar, Dr. X. Huang, Dr. Y. Lu, Dr. G. Chen, Dr. M. Wang, Dr. J. Liu, Dr. G. Zhang, Dr. M. Yu, Dr. H. Qi, Prof. Dr. X. Feng, Prof. Dr. R. Dong
Center for Advancing Electronics Dresden & Faculty of Chemistry and Food Chemistry, Technische Universität Dresden
Mommsenstrasse 4, 01062 Dresden (Germany)
E-mail: xinliang.feng@tu-dresden.de

Prof. W. Sun[+]
The Department of Basic Chemistry, The School of Pharmacy, Fujian Medical University
Fuzhou, Fujian 350108 (China)

Y. Jin,[+] Prof. Dr. G. Xu
State Key Laboratory of Structural Chemistry, Fujian Provincial Key Laboratory of Materials and Techniques toward Hydrogen Energy, Fujian Institute of Research on the Structure of Matter, Chinese Academy of Sciences
Fuzhou, Fujian 350002 (China)
E-mail: gxu@fjirsm.ac.cn

D. Mücke,[+] Dr. H. Qi, Prof. Dr. U. Kaiser
Central Facility for Materials Science Electron Microscopy, Universität Ulm
89081 Ulm (Germany)

Dr. Z. Liao
Fraunhofer Institute for Ceramic Technologies and Systems (IKTS)
Maria-Reiche-Strasse 2, 01109 Dresden (Germany)

Dr. G. Zhang, Prof. Dr. R. Dong
Key Laboratory of Colloid and Interface Chemistry of the Ministry of Education, School of Chemistry and Chemical Engineering, Shandong University
Jinan 250100 (China)
E-mail: renhaodong@sdu.edu.cn

Prof. Dr. X. Feng
Department of Synthetic Materials and Functional Devices, Max Planck Institute for Microstructure Physics
06120 Halle (Saale) (Germany)

[+] These authors contributed equally to this work.

plane extended π-conjugation have recently attracted intensive attention due to their high electrical conductivity and tailorable electronic band gaps.[8] During the last decade, extensive efforts have been dedicated to developing synthetic strategies for the construction of 2D *c*-MOFs, such as bulk-type crystals via solvothermal synthesis (most of the resultant bulk 2D *c*-MOFs exhibit needle-like morphologies due to the unbalanced interactions between strong in-plane coordination and weak out-plane π-stacking),[9] and polycrystalline films via surface- or interface-assisted synthesis[17–22]. Even though multiple sample forms have been achieved so far, the simultaneous realization of high porosity, high mass permeability, highly accessible active sites, and intrinsic conductivity in 2D *c*-MOFs has remained scarce due to their inherent micropores and densely layer-stacking structures, thus suppressing the mass transport properties and limiting device performance for energy and electronics.[10] In this respect, the design of hierarchically nanostructured 2D *c*-MOFs with tailorable morphologies, high porosity, and high crystallinity is crucial, which enables to endow electrically conductive 2D *c*-MOFs with superior mass transport properties for excellent energy and electronics applications.

The sacrificial template method has been regarded as a promising strategy for the controlled synthesis of hierarchical nanostructures,[11] which can precisely replicate the original templates and does not require an additional etching process.[12] Over the past few years, this strategy has been extensively used to synthesize three-dimensional (3D) MOFs with hierarchical structures that could further improve the porosity.[10b,13] However, despite the fact that the morphological control of 2D *c*-MOFs using the sacrificial template method has been less developed to date, the advances in the 3D MOFs synthesis by sacrificial templating have revealed an unfortunate trade-off on the low crystallinity due to the fast coordination reaction kinetics.[10b,14] Thus, the traditional sacrificial template strategy faces a grand challenge for 2D *c*-MOFs to achieve both hierarchical nanostructures and high crystallinity.

Herein, we present a template strategy for the general synthesis of hierarchically nanostructured 2D *c*-MOFs with high crystallinity, tailored morphologies, and high porosity via MOFs-to-*c*-MOFs transformations. Kinetics studies demonstrate that the insulating 3D MOFs are taken as primary templates and a generated amorphous intermediate layer on the 3D MOF surface acts as a unique secondary template, that determines the geometries of the resultant 2D *c*-MOFs and slows down the coordination reaction kinetics to enhance the crystallinity. The experimental and theoretical studies reveal that the thermodynamic driving force contributes to the formation of more stable coordination bonds, leading to spontaneous MOFs-to-*c*-MOFs transformations at room temperature. To demonstrate the generality of this template strategy, we have considered the use of different metals (Cu, Co, Ni, Zn, and bimetal Cu/Zn) and variable ligands (benzenehexathiol (BHT), hexahydroxybenzene (HHB), 2,3,6,7,10,11-hexaaminotriphenylene (HATP) and 2,3,6,7,10,11-hexahydroxytriphenylene (HHTP)). The resultant 12 different 2D *c*-MOFs present high crystallinity, encompassing different architectures (single shell, double shells and multi-shells), diverse dimensions (1D nanotubes, 2D nanosheets (NSs), and 3D nanocubes, nanospheres and nanoflowers as well as 3D NSs assembled frame film), and on variable substrates (carbon cloth, silicon wafer, and porous nylon 66 membrane). The hierarchical nanostructures of these 2D *c*-MOFs contribute to their high surface areas, improved mass transfer, and enhanced access to the active sites, making them ideal for energy storage and sensing applications. Thereby, we show that the hollow Cu-BHT nanocubes present an improved surface area of $94.8\ m^2 g^{-1}$ (≈ 41 times higher than that of the bulk Cu-BHT) and the integrated supercapacitor device reaches a specific capacity of $364.5\ F g^{-1}$ in organic electrolyte, 2.25-fold higher than that of bulk Cu-BHT counterparts. We further demonstrate that the Cu-HHB nanoflower-based chemiresistive sensor displays a 2.5-fold improvement in response intensity toward H_2S than the bulk-type Cu-HHB nanoparticles (NPs), which is one of the best room-temperature conductive polymer-based sensor devices for H_2S. We establish a breakthrough template strategy to realize a general transformation from insulating 3D MOFs to conductive 2D MOFs and are able to precisely tune the 2D *c*-MOFs for target energy and electronic device functions.

Results and Discussion

Representative 3D MOFs such as HKUST-1, CuBDC, and ZIF-8 feature weak metal-oxygen/metal-nitrogen coordination bonds that are unstable at the weakly acidic aqueous solution (e.g. pH = 5.0) or even under atmospheric conditions.[15] However, numerous 2D *c*-MOF crystals possess high chemical stability under an acidic environment and can maintain their crystal structures at pH = 3 aqueous solution (Figures S1–S3). Therefore, the square planar building units, MX_4 (M=Cu, Co, Ni, Zn; X=S, O and NH)[16] in 2D *c*-MOFs are supposed to be more stable than the weak coordination bonds in traditional 3D MOFs. Thus, the 3D insulating MOFs could be used as sacrificial templates for the synthesis of corresponding 2D *c*-MOFs crystals based on the thermodynamic driving force (Figure 1a). Density functional theory (DFT) calculations were further employed to explore the thermodynamic feasibility for the transformation of insulating 3D MOF precursors (including HKUST-1(Cu), Zn-BTC and ZIF-8(Zn) and ZIF-67(Co)) into 16 kinds of 2D *c*-MOFs (Figures 1b–1e). All the calculated Gibbs free energy change (ΔG) values of the MOFs-to-*c*-MOFs transformation reactions are less than zero at room temperature, suggesting that all the conversions are spontaneous in thermodynamics (Tables S1–S4). For the same 2D *c*-MOF product, the 3D MOF precursors with metal-nitrogen coordination bonds (M–N) exhibit more negative ΔG than those with metal-oxygen coordination bonds (M–O), suggesting that the M–N 3D MOFs are energetically preferred for transformation. For the same 3D MOF precursor, the calculated ΔG values of transformation mostly follow the order: $M(NH)_4$ *c*-MOFs < MS_4 *c*-MOFs < MO_4 *c*-MOFs, revealing that the possibility of the MOFs-to-

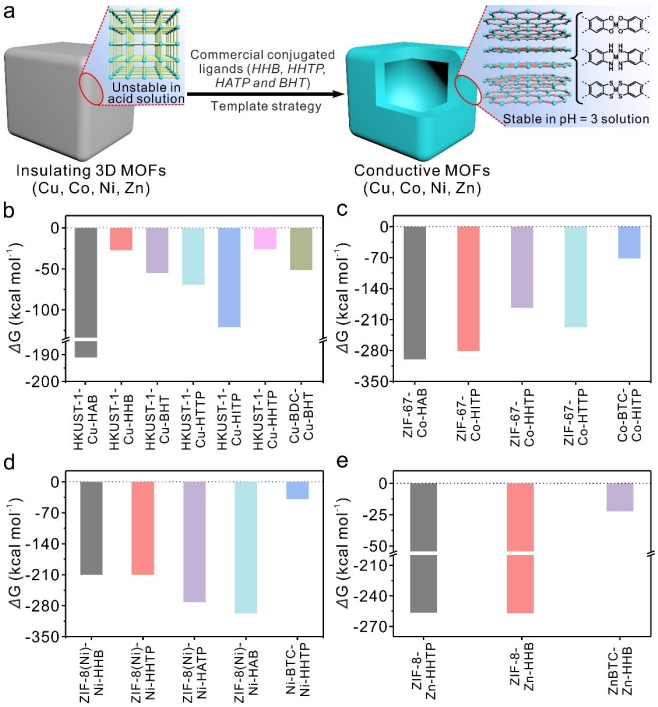

Figure 1. (a) Schematic overview of the transformation from insulating 3D MOFs precursors to 2D *c*-MOF samples. (b–e) Calculated Gibbs free energy change ($\triangle G$) for the transformation reaction from insulating 3D Cu-MOFs (HKUST-1, Cu-BDC), Co-MOFs (ZIF-67, Co-BTC), Ni-MOFs (ZIF-8-Ni, Ni-BTC) and Zn-MOFs (ZIF-8, Zn-BTC) precursors into corresponding 2D *c*-MOF samples, including Cu-HAB, Cu-HHB, Cu-BHT, Cu-HTTP, Cu-HITP, Cu-HHTP, Co-HAB, Co-HITP, Co-HHTP, Co-HTTP, Ni-HHB, Ni-HHTP, Ni-HATP, Ni-HAB, Zn-HHTP, and Zn-HHB.

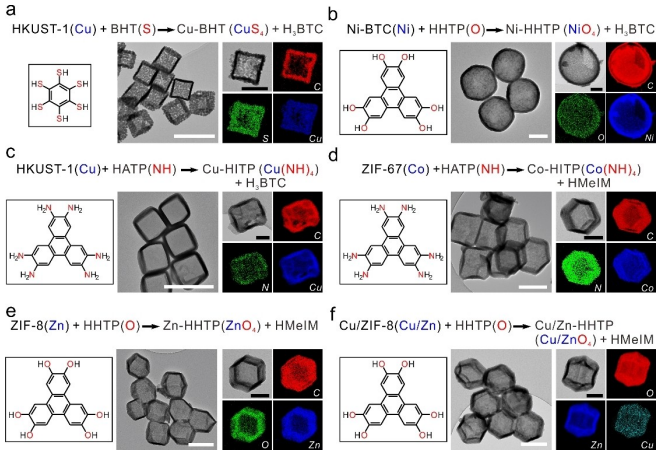

Figure 2. (a–f) Conjugated ligands (left), TEM images (middle) and the corresponding EELS mapping (right) of hollow Cu-BHT nanocubes, hollow Ni-HHTP NPs, hollow Cu-HITP nanocubes, hollow Co-HITP NPs, hollow Zn-HHTP NPs and hollow Cu/Zn-HHTP NPs, respectively. Scale bars represent 500 nm for middle TEM images and 200 nm for right TEM images.

c-MOFs transformation follows the order of $M(NH)_4$ *c*-MOFs > MS_4 *c*-MOFs > MO_4 *c*-MOFs.

The hierarchical 2D *c*-MOFs were synthesized via a template method based on known 3D MOFs such as HKUST-1 and ZIFs. In a typical conversion of HKUST-1 (Cu) to hollow Cu-BHT nanocubes (Figure 2a), the cubic HKUST-1 was firstly synthesized as described previously[17] (Figure S4a), and then dispersed in the BHT solution (methanol: water = 7:1, v/v) at room temperature. HKUST-1 nanocubes could be completely converted into dark purple Cu-BHT nanocubes after 1 h (Figure 2a and Figures S4–S5). As shown in the scanning electron microscopy (SEM) and transmission electron microscopy (TEM) images, the Cu-BHT samples exhibit hierarchical hollow nanostructure (Figures S4b–4c). The high-resolution TEM (HRTEM) image reveals that the hollow Cu-BHT nanocubes are polycrystalline while the lattice fringe with the d-space of 0.34 nm should be attributed to the (001) plane[6] (Figure S4d). The corresponding electron energy loss spectroscopy (EELS) mapping indicated a homogeneous distribution of Cu, C and S elements over the hollow Cu-BHT nanocubes (Figure 2a). The Brunauer – Emmett – Teller (BET) surface area of the hollow Cu-BHT nanocubes was measured as 94.8 $m^2 g^{-1}$, which was ≈41 times higher than that of the bulk-type Cu-BHT NPs (2.3 $m^2 g^{-1}$) via traditional solvothermal synthesis (Figures S5–S7).

Following a similar transformation procedure, we further synthesized 5 kinds of hierarchical 2D *c*-MOFs via engineering the MOF precursors and conjugated ligands. The insulating 3D MOFs with different metals such as HKUST-1(Cu), Ni-BTC(Ni), ZIF-67(Co), and ZIF-8(Zn) were reacted with different conjugated ligands including HATP and HHTP. As a consequence, the 2D *c*-MOFs with different square planar linkages were constructed, such as hollow Ni-HHTP (NiO_4) NPs (Figure 2b), hollow Cu-HITP ($Cu(NH)_4$) NPs (Figure 2c), hollow Co-HITP ($Co(NH)_4$) NPs (Figure 2d) and hollow Zn-HHTP (ZnO_4) NPs (Figure 2e), which could be completely identified by SEM, TEM and X-ray diffraction measurements (Figures S8–S15). Furthermore, we demonstrated the synthesis of bimetallic Cu/Zn-HHTP with the Cu^{2+}-doped ZIF-8 as a sacrificial template (Figure 2f, Figures S16–S17). The corresponding EELS mappings reveal the homogeneous spatial distributions of metal elements (Cu^{2+} and Zn^{2+}) over the hollow Cu/Zn-HHTP NPs (Figure 2f). We have discovered that the speed of transformation is dependent on the coordination strength between the metals and coordinating atoms. It is notable that M–NH (HATP) and M–S (BHT) exhibited faster transformation rates than M–O (HHB, HHTP), which is consistent with the DFT calculation results. For example, a complete transformation from HKUST-1 to hollow Cu-HITP NPs took 30 min while 24 h was required for a complete ZIF-8 to hollow Zn-HHTP NPs conversion.

To establish a fundamental understanding of the transformation of 3D MOFs into hierarchical 2D *c*-MOFs, time-dependent TEM and X-ray diffraction were employed to monitor the crystalline phase transitions. Herein the ZIF-8 to hollow Zn-HHTP NPs transformation was taken as a representative example (Figure 3, Figures S18–S19). We observed an amorphous Zn-HHTP layer (≈20 nm thick-

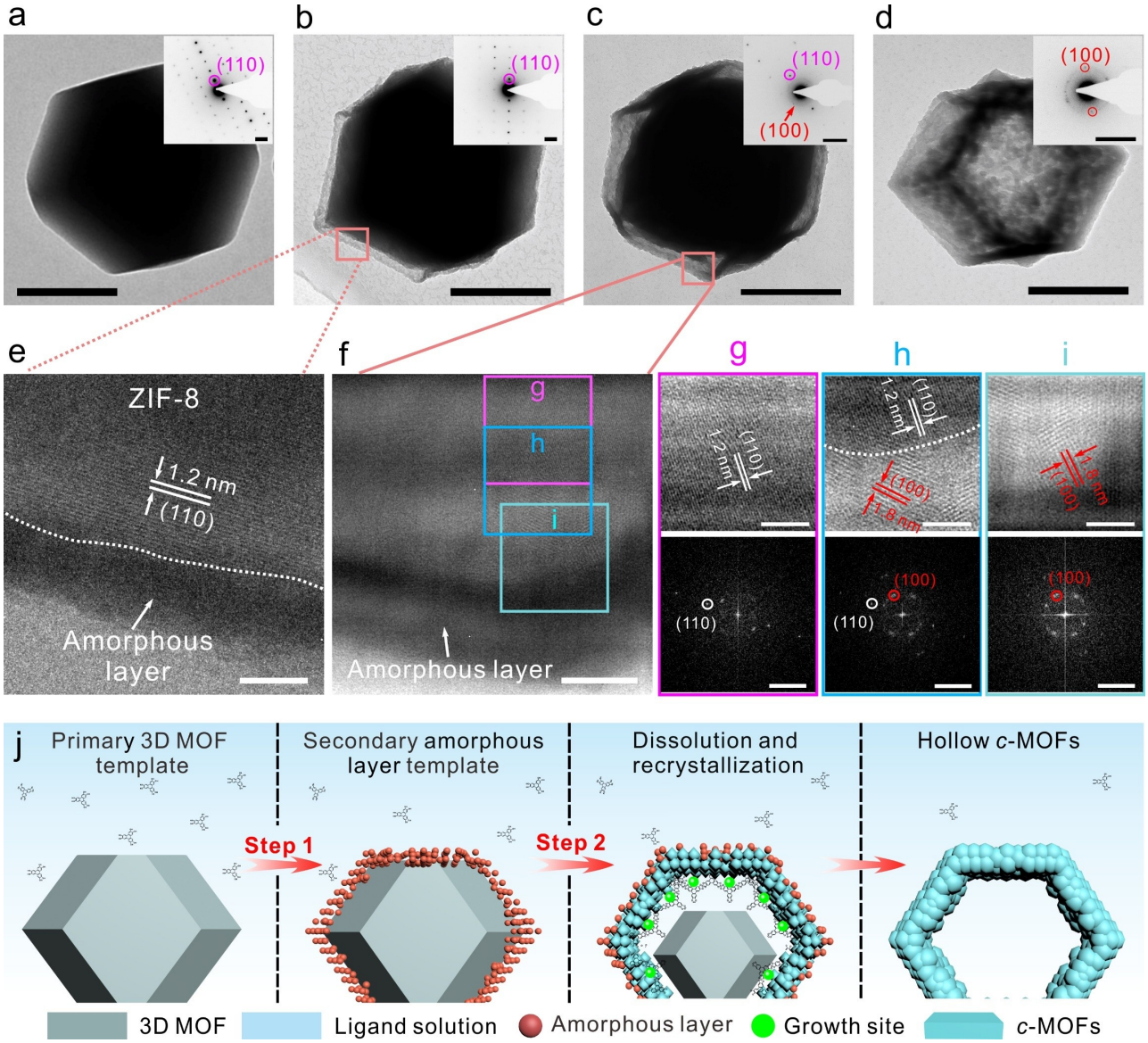

Figure 3. (a–d) TEM images of the samples transformed from ZIF-8 NPs with the reaction time of (a) 0 min, (b) 10 min, (c) 30 min and (d) 24 h. The inset images are the corresponding SAED patterns. (e) HRTEM images of the samples at 10 min. The interface between ZIF-8 and amorphous Zn-HHTP in (b) is highlighted by white dashed lines. (f) HRTEM images of the samples at 30 min. (g–i) Enlarged HRTEM images (top) and the corresponding Fourier transform patterns (bottom) of the selected areas in (f). The interface between ZIF-8 and crystallized Zn-HHTP in (h) is highlighted by white dashed lines. Scale bars represent 200 nm for (a–d), 20 nm for (e), 50 nm for (f), 20 nm for (g–i), and 1 1/nm for the inset SAED and FFT images. (j) Schematic overview of the two-stepped transformation mechanism of ZIF-8 NPs to hollow Zn-HHTP NPs.

ness) firstly formed on the surface of the ZIF-8 template within 10 minutes of the reaction (Figures 3a–3b and 3e, Figure S20). With the reaction proceeded (at 30 min), polycrystalline Zn-HHTP was observed while the ZIF-8 core was gradually hollowing (Figures 3c and 3f, Figure S21). After 24 h, the crystalline Zn-HHTP formed finally while the ZIF-8 core completely disappeared (Figure 3d, Figure S22). In the cross-sectional specimen of the sample at 30 min, the three sites (g, h, i) selected in a nearly radial direction were notably different in their crystalline states (Figure 3f). Site g exhibits a highly crystallized ZIF-8 core, whereas site i, located close to the amorphous layer, displays polycrystalline Zn-HHTP (Figures 3g and 3i). The intermediate site i represents a transition zone, characterized by a discernible borderline (illustrated by a white dashed line) between the ZIF-8 core and polycrystalline Zn-HHTP regions (Figure 3h). We anticipated that this border would move further inward with increasing reaction time, owing to the Kirkendall effect.[18] Additionally, crystalline phases were also observed outside the surface of the amorphous shell while the amorphous intermediate layer itself decomposed (Figure S21a-S21b and S21e), as a result of the conversion of the kinetically unstable amorphous phase into a stable crystalline phase.[19]

Based on the aforementioned experimental results, a possible two-step "template mechanism" is proposed to

illustrate the transformation (Figure 3j). In the first step, an amorphous *c*-MOFs intermediate layer quickly forms on the surface of the 3D MOFs template due to the initial fast reaction kinetics. This amorphous layer acts as a unique secondary template for the subsequent processes. The second step involves simultaneous dual processes: heterogeneous nucleation and growth of crystalline *c*-MOFs within the secondary amorphous template, and the spontaneous dissolution of the 3D MOFs core. During the transformation, the amorphous layer is supposed to serve as nucleation and growth sites, as well as a barrier to reduce the reaction kinetics between ligands in solution and metal ions inside the layer. To verify this hypothesis, we conducted molecular dynamics (MD) simulation models of the reaction process of HHTP molecules and Zn^{2+} ions with/without the presence of secondary template (Figures 4a-4b, Figure S23). Our simulations demonstrate that in the absence of the amorphous layer, HHTP molecules and Zn^{2+} ions rapidly aggregate (Figure 4a, 4c and Figure S23). The growth sites are always changing and mainly depending on the mass diffusion (Figure 4d). However, when the amorphous layer is involved, the reaction speed of HHTP molecules and Zn^{2+} ions is significantly reduced (Figures 4b, 4c). Moreover, the growth sites are located on the surface of the amorphous template (Figure 4d). In a control experiment, the formation of the amorphous layer was disrupted by the ultrasonication process, resulting in 2D *c*-MOFs with non-uniform sheet-like/needle-like aggregates under otherwise identical reaction conditions (Figure S24).

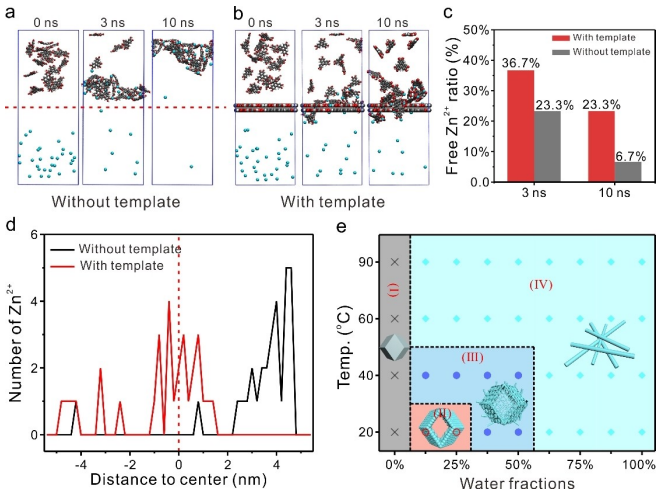

Figure 4. (a, b) Schematic molecular dynamics simulation models depicting the reaction process of HHTP molecules and Zn^{2+} ions with/without the presence of amorphous layer at time of 0 ns, 3 ns and 10 ns. (c) The ratios of free Zn^{2+} ions at the time of 3 ns and 10 ns. (d) Density distribution of Zn^{2+} ions alongxcoordinate in the dynamic structure at time of 10 ns. (e) Phase diagram illustrating the correlation between the solvent composition (horizontal ordinate) and reaction temperature (vertical ordinate). zone (I): pure ZIF-8 NPs; zone (II): hollow Zn-HHTP NPs; zone (III): Zn-HHTP nanowires assembled frame, as a transition stage between zone (II) and zone (IV); zone (IV): monodispersed Zn-HHTP nanowires.

The reaction kinetics was also found to play a vital role in the morphologies of the final 2D *c*-MOF samples during the transformation (Figure 4e, Figure S25). At low water fraction and low-temperature conditions (e.g. 12.5 % and 20 °C), the low etching rate of ZIF-8 allowed the formation of complete secondary template that fully covered the ZIF-8 (zone (II) in Figure 4e, Figure S25a, S25d). The nucleation and growth of Zn-HHTP occurred primarily on the inner wall of the Zn-HHTP shell (Figure S25g). With higher water fraction and temperature (e.g. 37.5 % and 40 °C), the increased etching rate of ZIF-8 hindered the complete coverage of the secondary template, leading to the diffusion of a small portion of Zn^{2+} ions into the solution (Figures S25b, S25e, and S26). This resulted in the formation of a few needle-like Zn-HHTP crystals outside the shell (zone (III) in Figure 4e, Figure S24h). If the water fraction and temperatures were further increased (e.g. 75 % and 60 °C), the etching rate of ZIF-8 is much faster than the formation rate of a secondary template (Figures S25c, S25f). As a result, Zn^{2+} ions diffused into the solution and reacted with deprotonated ligands to produce needle-like Zn-HHTP nanowires in the solution (zone (IV) in Figure 4e, Figure S25i, S26).

Despite the development of many 2D c-MOFs with diverse crystal and topological structures, controlling the sizes and shapes of these materials, particularly at room temperature and without the addition of surfactants, remains a significant challenge. Herein, we have also extended the proposed template strategy to the fabrication of highly crystalline 2D *c*-MOFs with different nanoarchitectures, dimensions, and on various substrates.

Using 3D MOFs as sacrificial-template, 2D *c*-MOFs with double-shelled hollow and hollow multishelled structures can be achieved. An interesting "shell-in-shell" 2D c-MOF was synthesized via the use of ZIF-67@ZIF-8 NPs as sacrificial templates (Figure 5a, Figures S27–S28). The corresponding EELS mappings confirm that Zn^{2+} is uniformly distributed over the outer shell, while Co^{2+} is distributed on the inner shell of double-shelled hollow Co-HHTP@Zn-HHTP NPs (Figure S27e). When using HKUST-1 NPs with large sizes of ≈1.5 μm as precursors, hollow Cu-BHT NP features with multiple shells were constructed (Figure 5b, Figures S29–S31).

Apart from the 0D hollow 2D *c*-MOFs NPs, 2D *c*-MOFs with 1D nanotubes (Figure 5c), 2D dimensional NSs (Figure 5d), 3D nanoflowers (Figure 5e) and 3D NSs-assembled frame film (Figure 5f) nanoarchitectures could also be achieved by the proposed strategy. Herein Zn-HHB nanotubes were easily obtained by selecting Zn-BTC(Zn) nanowires as the 3D MOF precursors (Figure S32a). The resulting 1D Zn-HHB samples feature a hollow nature with a polycrystalline wall thickness of about 20 nm (Figure 5c, Figures S32–S33). Furthermore, by using square CuBDC NSs as a precursor, 2D CuBHT NSs were obtained, with a thickness of approximately 7 nm and lateral dimensions of 1.0–5.0 μm (Figure 5d, Figures S34–S35). Notably, 2D *c*-MOFs with complex architectures can also be obtained (Figures 5e–5f). In this study, the Cu-HHB nanoflowers and Cu-BHT NSs-assembled frame films are constructed. As

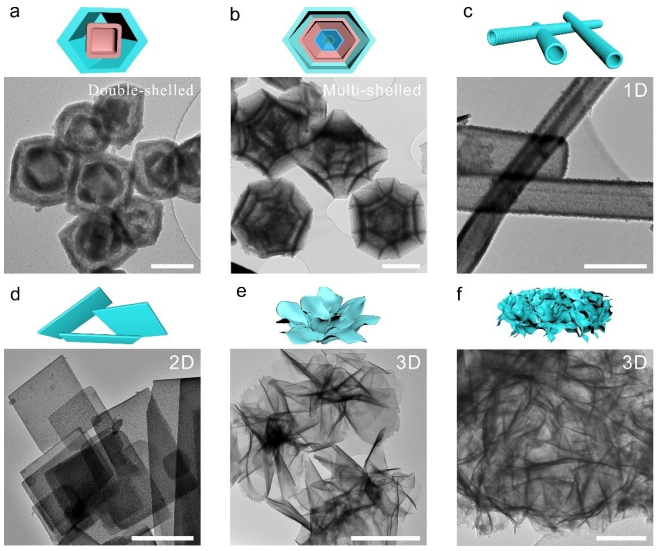

Figure 5. (a–f) TEM images of double-shelled hollow Co-HHTP@Zn-HHTP NPs, hollow multishelled CuBHT NPs, Zn-HHB nanotubes, CuBHT NSs, Cu-HHB nanoflowers, Cu-BHT NSs-assembled frame nanofilm, respectively. Scare bars represent 500 nm for (a), 1 μm for (b–d, f), 200 nm for (e).

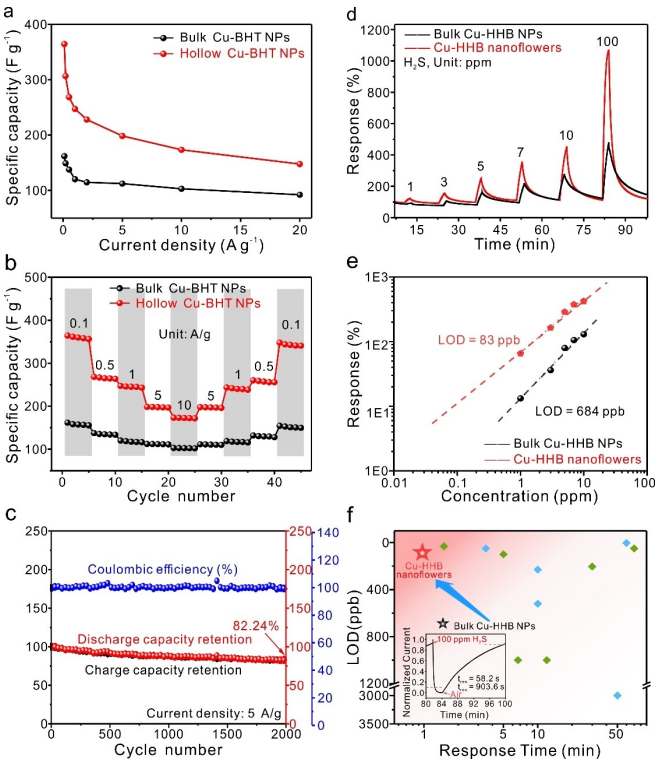

Figure 6. (a) Specific capacitance comparison at different current density between bulk and hollow CuBHT NPs. (b) Rate performance comparison between bulk and hollow CuBHT NPs. (c) Cycling performance and coulombic efficiencies of the hollow CuBHT sample at a current density of 5 $A g^{-1}$. (d) Response of Cu-HHB-based sensors to different H_2S concentration at room temperature. (e) Linear double logarithmic curve of the response and concentration of Cu-HHB-based sensors. (f) Comparison with other reported conductive polymer H_2S sensing materials at room temperature. (see Supporting Information Table S8 for details, Inset was the response-recovery time curve of Cu-HHB nanoflowers under 100 ppm H_2S, blue represented irrecoverable sensing materials, green represented recoverable sensing materials.)

corroborated by X-ray diffraction, SEM and TEM, both the Cu-HHB and Cu-BHT nanofilms are composed of polycrystalline nanosheets and exhibit flower-like and honeycomb-like nanoarchitecture, respectively (Figures S36–S39).

Moreover, based on the proposed template strategy, the hierarchical 2D *c*-MOFs can be fabricated onto different substrates, such as carbon fibre, silicon wafer, and porous membranes, enabling their practical integrations in energy storage and sensing devices. Herein, by converting ZIF-8 to hollow Zn-HHTP NPs, conductive Zn-HHTP nanofilms were grown on various substrates, including brush-like Zn-HHTP nanowire films on carbon nanofiber, hollow Zn-HHTP films on the silicon wafer, and hollow Zn-HHTP films on nylon 66 membrane (s S40–S42).

Compared to the insulating 3D MOFs precursors, the as-prepared 2D *c*-MOFs samples possess intrinsic electrical conductivity that ranges from approximately 10^{-6} to 10^{2} $S cm^{-1}$ (Table S5). It is notable that all the 2D *c*-MOFs formed by transformation exhibit high crystallinity and hierarchical nanoarchitectures. These 2D *c*-MOFs exhibit ≈1.3–62.1 times higher BET surface area than those of reported bulk-type 2D *c*-MOFs (Table S6), which would facilitate mass transportation and improve access to the redox active sites. To illustrate the application potentials of these achieved 2D *c*-MOFs, we first integrated the Cu-BHT hollow nanocubes into a supercapacitor for electrochemical energy storage. The bulk-type 2D *c*-MOFs samples synthesized by the conventional solvothermal method were employed as references.[20]

The supercapacitor performance of our hollow Cu-BHT nanocubes versus bulk-type Cu-BHT NPs was demonstrated in Figures 6a–6c. The charge storage behavior of hollow CuBHT and bulk-type samples were conducted in 1 M tetraethylammomium tetrafluoroborate/acetonitrile organic electrolyte with a three-electrode system. X-ray diffraction and X-ray photoelectron spectroscopy reveals that the bulk-type and hollow CuBHT NPs feature identical crystal structures and compositions (Figure S5–S7 and S43). Moreover, according to the cyclic voltammetry (CV) results, they exhibit similar rectangular shapes with one pair of redox peaks in a potential range of −0.6 to 0.6 V and detailed analysis could be found in Supporting Information (Figures S44–S45). Compared to the bulk-type CuBHT (161.92 $F g^{-1}$), the specific capacity of hollow CuBHT nanocubes increased dramatically by 125.11 %, reaching 364.5 $F g^{-1}$ at a current density of 0.1 $A g^{-1}$ (Figures 6a-6b, Figures S44b, S45b). This value is superior to those of recently reported MOF-based electrode materials, porous carbon, graphene and MXenes (Table S7). This decent capacity improvement should be ascribed to the increased BET surface area (94.8 and 2.3 $m^2 g^{-1}$ for hollow Cu-BHT nanocubes and bulk Cu-BHT NPs, respectively) and more exposed redox sites of hollow Cu-BHT nanocubes. Even after experiencing a charge/discharge process for 2000 cycles, the capacity retention of hollow CuBHT nano-

cubes could still reach 82.24 %, suggesting the good electrochemical cycling stability of the transformed CuBHT nanocubes (Figure 6c, Figures S46).

The chemiresistive gas sensing properties of our Cu-HHB nanoflowers-versus bulk Cu-HHB NPs-based chemiresistor towards H_2S at room temperature is demonstrated in Figures 6d-6f (Figures S36–S37 and S47–S49). Upon exposure to H_2S, the resistance of both the nanoflowers and NPs distinctly increased, and then recovered to the initial value after purging with air (Figure 6d, Figures S50–S51), indicating that Cu-HHB redox active sites and semiconducting properties were undamaged by H_2S.[21] The response intensity of Cu-HHB nanoflowers to 100 ppm H_2S was 978 %, which represents a 2.5-fold improvement compared to the bulk-type Cu-HHB NPs (Figure 6d).

The response-concentration log–log plots of Cu-HHB bulk and nanoflowers derived from Figure 4d showed a good linear relationship in the range of 1–100 ppm. Notably, Cu-HHB nanoflowers exhibited a theoretical limit of detection (LOD) of 83 ppb by setting $R = 10$ %, representing an 8-fold optimization compared to Cu-HHB bulk (Figure 6e). Furthermore, Cu-HHB nanoflowers showed a faster response time of 58.2 s to 100 ppm H_2S, which was 2.1 times faster than the response time of bulk material (124.8 s) (Figure 6f, Figure S52). It is notable that Cu-HHB nanoflowers ranked in the best conductive polymer-based sensing materials (including MOFs, covalent organic framework, and organic polymer. et al.) for H_2S sensing at room temperature with the fastest response speed and one of the lowest LOD values (Figure 6f, Table S8). Compared to bulk Cu-HHB NPs, the excellent gas sensing performance can be attributed to the increased BET surface area of Cu-HHB nanoflowers (130.2 $m^2 g^{-1}$ vs 311.5 $m^2 g^{-1}$) for more efficient gas enrichment, ultrathin 2D nanosheet morphology for faster mass transport, and higher utilization ratio of inner active sites. Moreover, Cu-HHB nanoflowers-based gas sensor displayed outstanding repeatability, selectivity, and long-term stability towards H_2S (Figures S53–S56).

Conclusion

In summary, we have developed a versatile and efficient template strategy for the synthesis of highly crystalline 2D *c*-MOFs with hierarchical nanostructures. Families of 2D *c*-MOFs with varying chemical compositions, different shells, diverse dimensions, and on variable substrates have been achieved by controllable synthesis. The transformation from 3D MOFs to 2D *c*-MOFs is driven by the thermodynamical mechanism of forming more stable coordination bonds in the 2D *c*-MOFs compared to the 3D MOFs precursors. This transformation takes advantage of a unique secondary template created by an amorphous intermediate layer, resulting in final samples with highly morphology-dependent properties. Additionally, the crystallinity is maximized by slowing down the coordination rate and suppressing disordered stacking. The resultant hierarchical 2D *c*-MOFs exhibited high electrical conductivity and large specific surface areas, making them ideal for energy storage and sensing applications. Impressively, the as-synthesized hollow Cu-BHT nanocubes-based supercapacitor and Cu-HHB nanoflowers based chemiresistive gas sensor achieved 2.25-fold and 2.5-fold improvement in capacity and response intensity, respectively, over traditional bulk-type 2D *c*-MOFs. Therefore, the demonstrated template strategy will not only extend generality, tunability and scalability of 2D *c*-MOFs synthesis but also drive advancements in both fundamental and application researches for 2D *c*-MOFs.

Acknowledgements

This work was financially supported by ERC starting grant (FC2DMOF, No. 852909), ERC Consolidator Grant (T2DCP), CRC 1415 (Chemistry of Synthetic Two-Dimensional Materials, No. 417590517), GRK2861 (No. 491865171), as well as the German Science Council and Center of Advancing Electronics Dresden (cfaed). R.D. thanks Taishan Scholars Program of Shandong Province (tsqn201909047), Natural Science Foundation of Shandong Province (ZR2023JQ005) and National Natural Science Foundation of China (22272092). C.H. gratefully acknowledges funding from the Alexander von Humboldt Foundation. We acknowledge Dresden Center for Nanoanalysis (DCN) at TUD and Dr. Petr Formanek (Leibniz Institute for Polymer Research, IPF, Dresden) for the use of facilities. Open Access funding enabled and organized by Projekt DEAL.

Conflict of Interest

The authors declare no conflict of interest.

Data Availability Statement

The data that support the findings of this study are available from the corresponding author upon reasonable request.

Keywords: Chemiresistive Sensor · Conductive 2D MOFs · Hierarchical Nanostructure · Supercapacitor · Template Strategy

[1] a) D. Feng, T. Lei, M. R. Lukatskaya, J. Park, Z. Huang, M. Lee, L. Shaw, S. Chen, A. A. Yakovenko, A. Kulkarni, *Nat. Energy* **2018**, *3*, 30–36; b) D. Sheberla, J. C. Bachman, J. S. Elias, C.-J. Sun, Y. Shao-Horn, M. Dincă, *Nat. Mater.* **2017**, *16*, 220–224.

[2] Y. Lu, Y. Zhang, C.-Y. Yang, S. Revuelta, H. Qi, C. Huang, W. Jin, Z. Li, V. Vega-Mayoral, Y. Liu, *Nat. Commun.* **2022**, *13*, 7240.

[3] L. Yang, P. Cai, L. Zhang, X. Xu, A. A. Yakovenko, Q. Wang, J. Pang, S. Yuan, X. Zou, N. Huang, Z. Huang, H.-C. Zhou, *J. Am. Chem. Soc.* **2021**, *143*, 12129–12137.

[4] a) Z. Meng, A. Aykanat, K. A. Mirica, *J. Am. Chem. Soc.* **2019**, *141*, 2046–2053; b) M. G. Campbell, D. Sheberla, S. F. Liu, T. M. Swager, M. Dincă, *Angew. Chem. Int. Ed.* **2015**, *54*, 4349–

4352; c) C. Huang, X. Shang, X. Zhou, Z. Zhang, X. Huang, Y. Lu, M. Wang, M. Löffler, Z. Liao, H. Qi, *Nat. Commun.* **2023**, *14*, 3850; d) P. Chen, X. Su, C. Wang, G. Zhang, T. Zhang, G. Xu, L. Chen, *Angew. Chem. Int. Ed.* **2023**, *62*, e202306224.
[5] X. Yan, X. Su, J. Chen, C. Jin, L. Chen, *Angew. Chem. Int. Ed.* **2023**, *62*, e202305408.
[6] X. Huang, S. Zhang, L. Liu, L. Yu, G. Chen, W. Xu, D. Zhu, *Angew. Chem. Int. Ed.* **2018**, *130*, 152–156.
[7] a) S. Takaishi, M. Hosoda, T. Kajiwara, H. Miyasaka, M. Yamashita, Y. Nakanishi, Y. Kitagawa, K. Yamaguchi, A. Kobayashi, H. Kitagawa, *Inorg. Chem.* **2009**, *48*, 9048–9050; b) A. A. Talin, A. Centrone, A. C. Ford, M. E. Foster, V. Stavila, P. Haney, R. A. Kinney, V. Szalai, F. El Gabaly, H. P. Yoon, *Science* **2014**, *343*, 66–69; c) T. C. Narayan, T. Miyakai, S. Seki, M. Dincă, *J. Am. Chem. Soc.* **2012**, *134*, 12932–12935.
[8] a) H. Zhong, M. Wang, G. Chen, R. Dong, X. Feng, *ACS Nano* **2022**, *16*, 1759–1780; b) M. Wang, R. Dong, X. Feng, *Chem. Soc. Rev.* **2021**, *50*, 2764–2793; c) R. Dong, P. Han, H. Arora, M. Ballabio, M. Karakus, Z. Zhang, C. Shekhar, P. Adler, P. S. Petkov, A. Erbe, *Nat. Mater.* **2018**, *17*, 1027–1032; d) M. Hmadeh, Z. Lu, Z. Liu, F. Gándara, H. Furukawa, S. Wan, V. Augustyn, R. Chang, L. Liao, F. Zhou, *Chem. Mater.* **2012**, *24*, 3511–3513.
[9] a) J.-H. Dou, M. Q. Arguilla, Y. Luo, J. Li, W. Zhang, L. Sun, J. L. Mancuso, L. Yang, T. Chen, L. R. Parent, *Nat. Mater.* **2021**, *20*, 222–228; b) G. Skorupskii, B. A. Trump, T. W. Kasel, C. M. Brown, C. H. Hendon, M. Dincă, *Nat. Chem.* **2020**, *12*, 131–136.
[10] a) Y. Chen, Q. Zhu, K. Fan, Y. Gu, M. Sun, Z. Li, C. Zhang, Y. Wu, Q. Wang, S. Xu, *Angew. Chem. Int. Ed.* **2021**, *133*, 18917–18924; b) W. Cheng, H. Zhang, D. Luan, X. W. Lou, *Sci. Adv.* **2021**, *7*, eabg2580.
[11] a) Z.-Y. Wu, P. Zhu, D. A. Cullen, Y. Hu, Q.-Q. Yan, S.-C. Shen, F.-Y. Chen, H. Yu, M. Shakouri, J. D. Arregui-Mena, A. Ziabari, A. R. Paterson, H.-W. Liang, H. Wang, *Nat. Synth.* **2022**, *1*, 658–667; b) Y. Li, W. Zhou, I. Tanriover, W. Hadibrata, B. E. Partridge, H. Lin, X. Hu, B. Lee, J. Liu, V. P. Dravid, K. Aydin, C. A. Mirkin, *Nature* **2022**, *611*, 695–701; c) A. M. Evans, A. Giri, V. K. Sangwan, S. Xun, M. Bartnof, C. G. Torres-Castanedo, H. B. Balch, M. S. Rahn, N. P. Bradshaw, E. Vitaku, D. W. Burke, H. Li, M. J. Bedzyk, F. Wang, J.-L. Brédas, J. A. Malen, A. J. H. McGaughey, M. C. Hersam, W. R. Dichtel, P. E. Hopkins, *Nat. Mater.* **2021**, *20*, 1142–1148; d) D. Yu, Q. Shao, Q. Song, J. Cui, Y. Zhang, B. Wu, L. Ge, Y. Wang, Y. Zhang, Y. Qin, *Nat. Commun.* **2020**, *11*, 927.
[12] a) Y. Feng, Y. Ji, Y. Zhang, Q. Shao, Y. Xu, Y. Li, X. Huang, *Nat. Synth.* **2022**, *1*, 626–634; b) J. Nai, B. Y. Guan, L. Yu, X. W. Lou, *Sci. Adv.* **2017**, *3*, e1700732.
[13] H. Huang, J.-R. Li, K. Wang, T. Han, M. Tong, L. Li, Y. Xie, Q. Yang, D. Liu, C. Zhong, *Nat. Commun.* **2015**, *6*, 8847.
[14] W. Cheng, Z. P. Wu, D. Luan, S. Q. Zang, X. W. Lou, *Angew. Chem. Int. Ed.* **2021**, *133*, 26601–26606.
[15] a) N. C. Burtch, H. Jasuja, K. S. Walton, *Chem. Rev.* **2014**, *114*, 10575–10612; b) C. Han, C. Zhang, N. Tyminska, J. R. Schmidt, D. S. Sholl, *J. Phys. Chem. C* **2018**, *122*, 4339–4348.
[16] J. Park, A. C. Hinckley, Z. Huang, D. Feng, A. A. Yakovenko, M. Lee, S. Chen, X. Zou, Z. Bao, *J. Am. Chem. Soc.* **2018**, *140*, 14533–14537.
[17] Q. Liu, J.-M. Yang, L.-N. Jin, W.-Y. Sun, *CrystEngComm* **2016**, *18*, 4127–4132.
[18] Y. Yin, R. M. Rioux, C. K. Erdonmez, S. Hughes, G. A. Somorjai, A. P. Alivisatos, *Science* **2004**, *304*, 711–714.
[19] P. J. Smeets, A. R. Finney, W. J. Habraken, F. Nudelman, H. Friedrich, J. Laven, J. J. De Yoreo, P. M. Rodger, N. A. Sommerdijk, *Proc. Natl. Acad. Sci. USA* **2017**, *114*, E7882–E7890.
[20] a) Z. Meng, C. G. Jones, S. Farid, I. U. Khan, H. M. Nelson, K. A. Mirica, *Angew. Chem. Int. Ed.* **2022**, *134*, e202113569; b) X. Huang, H. Yao, Y. Cui, W. Hao, J. Zhu, W. Xu, D. Zhu, interfaces, *ACS Appl. Mater.* **2017**, *9*, 40752–40759.
[21] M.-S. Yao, P. Wang, Y.-F. Gu, T. Koganezawa, H. Ashitani, Y. Kubota, Z.-M. Wang, Z.-Y. Fan, K.-I. Otake, S. Kitagawa, *Dalton Trans.* **2021**, *50*, 13236–13245.

Manuscript received: September 12, 2023
Accepted manuscript online: November 27, 2023
Version of record online: December 15, 2023